Volume 20 | Number 38 | 14 October 2018 | Pages 5649–5858

CrystEngComm

rsc.li/crystengcomm

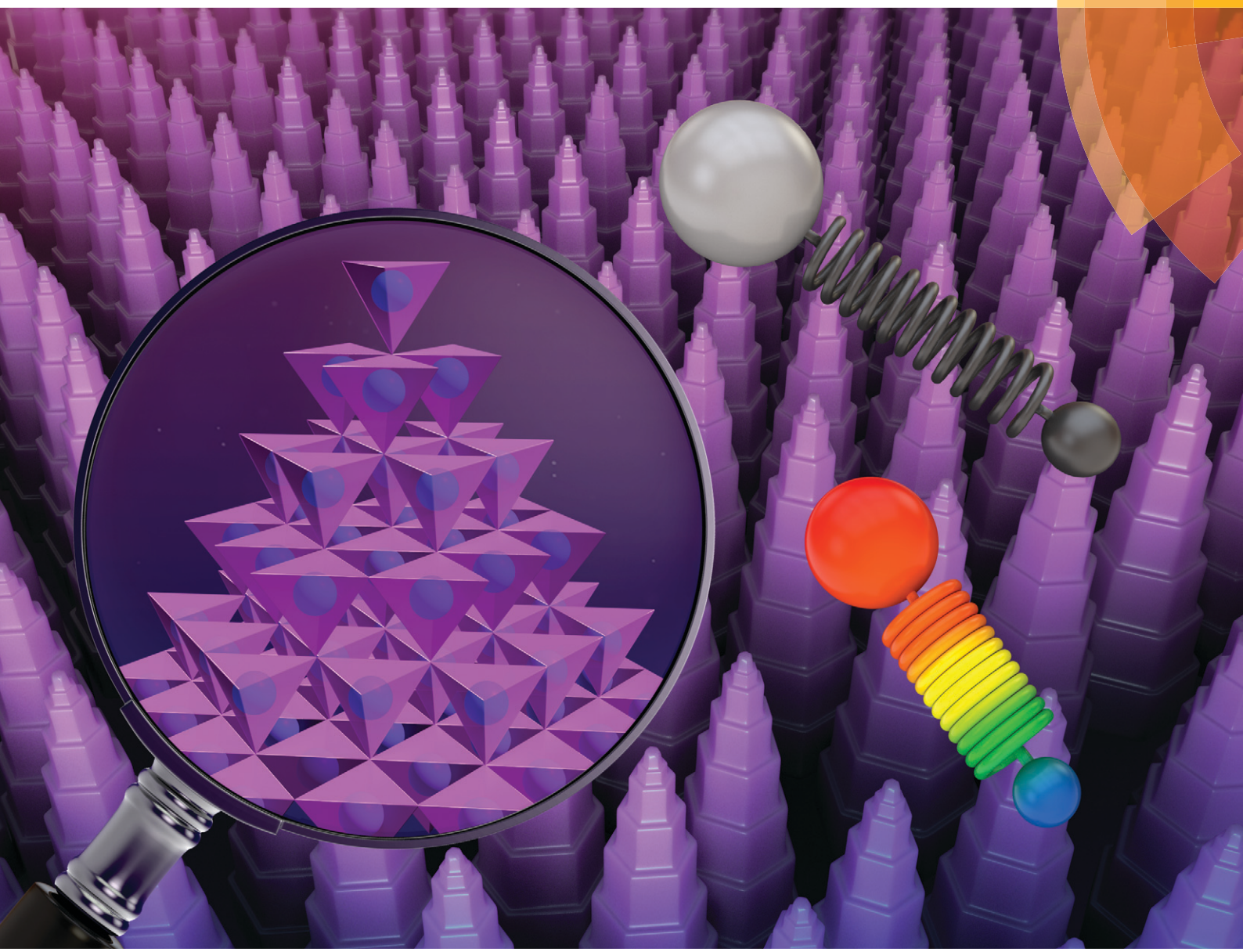

ROYAL SOCIETY OF CHEMISTRY

PAPER

A. A. Martinez-Morales *et al.*

Crystal growth and piezoelectric characterization of mechanically stable ZnO nanostructure arrays

CrystEngComm

PAPER

View Article Online
View Journal | View Issue

Cite this: *CrystEngComm*, 2018, **20**, 5688

Crystal growth and piezoelectric characterization of mechanically stable ZnO nanostructure arrays†

T. Lim, [a] G. Ico,[b] K. Jung, [ac] K. N. Bozhilov,[d] J. Nam [b] and A. A. Martinez-Morales *[a]

Received 15th May 2018,
Accepted 27th June 2018

DOI: 10.1039/c8ce00799c

rsc.li/crystengcomm

The highest piezoelectric performance of ZnO can be achieved by utilizing the piezoelectric operation along the *c*-axis due to its anisotropic permanent dipole moment. However, a 1-dimensional ZnO crystal is vulnerable to mechanical stress along the *c*-axis because it is susceptible to breaking. The synthesis of mechanically stable ZnO hexagonal, nanopyramidal arrays is achieved by modulating the premature oxidation of a Zn precursor on a fluorine-doped tin oxide (FTO) substrate during the chemical vapor depositon (CVD) process. The as-synthesized ZnO step-wise nanostructures show a piezoelectric charge coefficient of d_{33} = 13.20 pm V^{-1} measured by piezoresponse force microscopy (PFM). Post-synthesis annealing under an oxygen condition improves the piezoelectric response by 98% to a value of d_{33} = 26.10 pm V^{-1}. The growth mechanism, morphology, crystal structure, and crystal defects are characterized and discussed in this paper.

Introduction

Zinc oxide (ZnO) is a versatile material widely used as a pigment,[1] a UV absorber,[2] a purifier,[3] and an industrial additive.[4] ZnO interacts with UV light due to its wide direct bandgap (3.37 eV), allowing for its use in optoelectronic applications such as UV lasers,[5] UV detectors,[6] and blue LEDs.[7] In nature, the most stable structure of ZnO is hexagonal wurtzite, in which ZnO_4 tetrahedra share common corners. Furthermore, due to the absence of inversion symmetry in the wurtzite crystal, ZnO has piezoelectric properties.[8,9] Piezoelectricity is a property that allows the conversion of mechanical energy into electricity (or *vice versa*). Due to its piezoelectric properties, ZnO is suitable for cantilevers,[10] acoustic transducers,[11] and ultrasonic motor[12] applications. As part of the development of next generation renewable energy sources, the generation of electricity by the harnessing of mechanical energy can be achieved with a piezoelectric power generator. Currently, this application is being intensively researched on the micro- to nano-scale.[13,14]

Common materials with piezoelectricity are based on the working principle that randomly oriented ferroelectric domains are aligned by external forces, such as in the case of toxic $PbZrTiO_3$.[15] In contrast, ZnO has attracted much attention since it is a stable and environmentally friendly piezoelectric material. In the wurtzite ZnO structure, oxygen is displaced along the *c*-axis from its location in the ideal wurtzite ZnO, forming a dipole moment along the *c*-axis.[16] The most common operational modes in wurtzite ZnO are described by the piezoelectric charge coefficients, d_{33}, d_{31} and d_{15}. d_{33} describes the piezoelectric operational mode that has a response along the main axis where the dipole moment is formed against the mechanical stress applied along the main axis. d_{31} is the piezoelectric response along the main axis against the applied mechanical stress perpendicular to the main axis, and d_{15} is the response against shear stress.[17] It is known that, for ZnO, d_{33} is the highest piezoelectric charge coefficient, d_{33} = 12.3 pm V^{-1} (or pC/N), while the others, d_{31} = −5.12 pm V^{-1} and d_{15} = −8.3 pm V^{-1},[18] are lower in magnitude. Due to the highest piezoelectric charge coefficient, it is expected that the highest piezoelectric efficiency is achieved when the mechanical force is directed along the *c*-axis.

An important issue in piezoelectric power generation is how to efficiently collect the separated charges. A large part of the research on piezoelectric materials is based on quasi-low dimensional morphologies such as arrayed nanowire architectures,[19–21] since bulk materials are known to show lower piezoelectric performance.[22] The charges generated when the piezoelectric nanowire architecture is bent by an

[a] *College of Engineering – Center for Environmental Research and Technology, University of California – Riverside, Riverside, CA 92507, USA. E-mail: alfmart@ece.ucr.edu*
[b] *Department of Bioengineering, University of California – Riverside, Riverside, CA 92521, USA*
[c] *Department of Chemical and Environmental Engineering, University of California – Riverside, Riverside, CA 92521, USA*
[d] *Central Facility for Advanced Microscopy and Microanalysis, University of California – Riverside, Riverside, CA 92521, USA*

† Electronic supplementary information (ESI) available. See DOI: 10.1039/c8ce00799c

external mechanical stress are collected through an external circuit. However, because the charge separation is not formed along the main axis of the nanowire, there is an unavoidable efficiency loss in this type of device architecture.[23] To overcome structural limitations, piezoelectric nanowires have been laterally placed on stretchable substrates, where power generation is achieved by stretching the substrate.[24] This approach has obvious limitations in terms of achieving a high density of devices on a per area basis, creating opportunities for further investigating device architectures that can achieve higher efficiencies. To improve the density efficiency, vertically aligned 1-dimensional arrays are highly desirable. Unfortunately, the 1-dimensional nanowire structure is not ideal or even a suitable morphology because it is easily bent and broken by stress along its vertical axis. Therefore, the most suitable structure in terms of density and piezoelectric efficiency is an architecture where the main axis is vertically aligned and is stable against vertical stress. For higher mechanical stability, a vertically aligned tapered architecture is ideal in terms of performance and stability.

When Zn powder is used as the precursor material in the chemical vapor deposition (CVD) synthesis of ZnO, it was previously observed by our group[25] that the Zn precursor is prematurely oxidized at the precursor boat, forming a ZnO layer on top of the precursor that inhibits the continued evaporation of the Zn precursor, eventually blocking the process. Our synthesis technique is modified to modulate the amount of oxygen intake toward the precursor by using a test tube-shaped precursor boat to decrease the rate of Zn precursor supply slowly and control the reaction kinetics near the substrate. Through our developed method, highly packed, mechanically stable, vertically aligned hexagonal ZnO nanopyramidal structures were successfully synthesized on a FTO substrate. The piezoelectric properties of the synthesized ZnO were characterized by PFM. Post-synthesis annealing under oxygen conditions results in a 98% increase in d_{33} compared to the as-synthesized nanopyramid due to a decrease in crystal defects. The synthesis of ZnO on transparent substrates broadens its applicability on functional transparent coating materials, since both the ZnO product and substrate can be transparent.

Experimental

Materials

The FTO substrate (~8 Ω sq^{-1}, 80% transmittance) and Zn powder (99.995%, <150 μm) were purchased from Sigma-Aldrich. Nitrogen (99.999%) and oxygen (99.5%) were purchased from Praxair and Airgas, respectively. Hydrochloric acid (37% in water) was purchased from Acros Organics.

Instruments

A three-zone horizontal tube furnace (OTF-1200X-III, MTI Corporation) was used for ZnO CVD synthesis. The nitrogen gas flow was controlled and measured using an FM-1050 tube flow meter from Matheson Tri-Gas and a TopTrak 822 mass flow controller from Sierra Instruments, respectively. A CPX 2800 ultrasonic cleaner from Branson Ultrasonics was used for the ultrasonic cleaning. A KSL-1100X muffle furnace from MTI Corporation was used for the oxygen annealing treatment. FEI Nova NanoSEM 450 and Titan Themis 300 were used for scanning electron microscopy (SEM) and transmission electron microscopy (TEM), respectively. PANalytical Empyrean was utilized to characterize the crystal structure by X-ray diffraction (XRD) analysis. Piezoelectric force microscopy (PFM) was conducted using MFP-3D from Asylum Research with a highly conductive atomic force microscopy (AFM) cantilever (OMCL-AC240TM from Olympus). Horiba LabRAM was used for Raman spectroscopy. A Spex Fluorolog Tau-3 spectrophotometer was used for photoluminescence (PL) spectroscopy.

CVD synthesis of ZnO

The FTO substrate was precut to 2 × 2 cm^2 and cleaned by ultrasonication in detergent solution, acetone and 2-propanol for 15 min, respectively. 0.2 g Zn powder was loaded into a small quartz test tube and placed in a horizontal tube furnace. The prepared substrate was placed next to the test tube precursor boat. The tube furnace was purged by a mixture gas of 100 SCCM N_2 and 4 SCCM O_2 for 30 min under a low vacuum status using a mechanical pump to remove unintended gas impurities. The furnace was heated up to 450 °C for 30 min and maintained for another 30 min to allow the synthesis of ZnO. After the furnace cooled down, the ZnO synthesis was completed. To improve its piezoelectric properties, the as-synthesized ZnO on FTO was annealed under an oxygen condition in a muffle furnace. The muffle furnace was purged with 30 SCCM O_2 under atmospheric pressure for an hour, heated up to 500 °C and maintained for another hour. After the synthesis and annealing of ZnO was completed, some portion of the ZnO was removed using HCl to expose the underlying FTO surface for electrical connection and grounding.

Characterization

The synthesized ZnO was characterized in terms of morphology by SEM, crystal structure by XRD, crystal defect by TEM, PL and Raman spectroscopy, and piezoelectric properties by PFM. For the piezoelectricity measurement, the cantilever tip was placed at the apex of a pyramidal ZnO nanostructure. An electric field was applied and swept in the forms of triangle and alternating steps to measure the piezoelectric response from the sample. The mechanical stability of the synthesized ZnO pyramids was tested by ultrasonication.

Results and discussion

Morphology

Fig. 1 shows the morphology of the synthesized ZnO hexagonal nanopyramids in low- (Fig. 1a) and high-magnification (Fig. 1b). The ZnO hexagonal prism with a step-wise decreasing diameter forms the hexagonal pyramidal morphology. In the ZnO crystal growth, the (001) plane is perpendicular to the

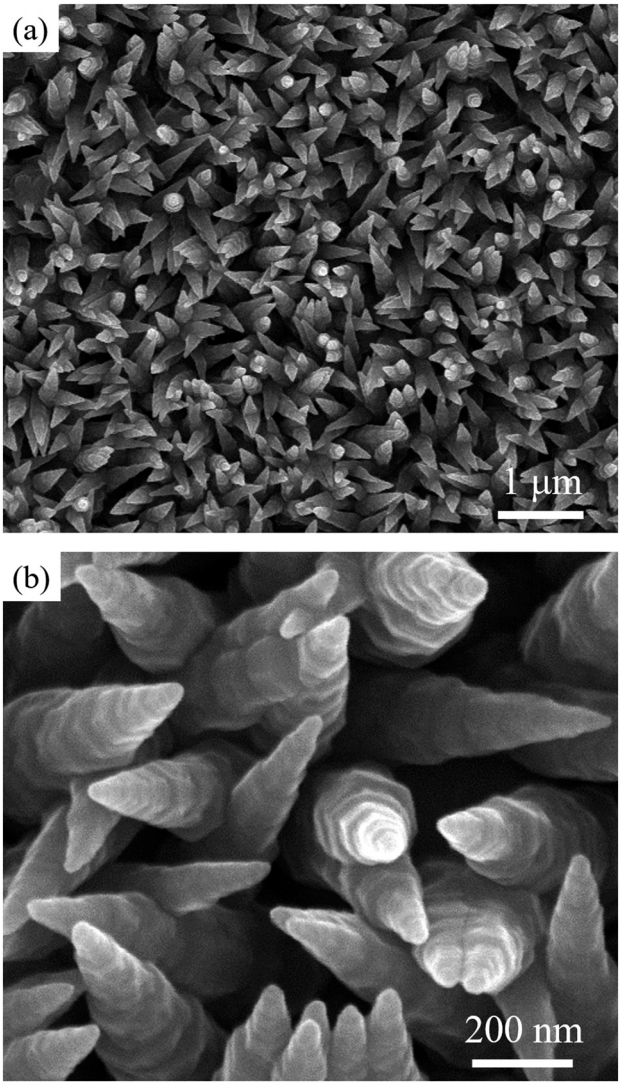

Fig. 1 Surface SEM image of the synthesized ZnO hexagonal pyramids under a magnification of (a) 20 000× and (b) 120 000×.

c-axis. This plane is a polar surface, while the other planes parallel to the *c*-axis are non-polar surfaces, in the hexagonal prismatic structure.[26] During synthesis, when the precursor is transported to the substrate, it tends to form an intermediate structure on the polar surface rather than the non-polar surfaces to reduce the surface energy.[27] This results in a directionally preferred growth in the ZnO crystal formation, with the growth rate along the *c*-axis faster than the other directions.[28]

In our modified CVD synthesis process (using a test tube-shaped precursor boat), positive pressure was generated by the evaporation of the Zn precursor at the deep end inside of the test tube. During the synthesis reaction, the positive pressure prevents oxygen from flowing into the test tube and prematurely oxidizing the Zn precursor material. The formation, morphology, and structural and physical characteristics of the synthesized hexagonal pyramidal nanostructures were controlled by the CVD reaction parameters (*e.g.* reaction temperature, flow gas ratio, pressure, *etc.*), as a direct function of the dimensions, geometry, and surface properties of the test tube precursor boat. By reducing the formation rate of the ZnO layer on top of the liquid Zn precursor, the flux of Zn(g) partial vapor pressure is controlled. The supply of the Zn precursor is slowly reduced, resulting in the formation of hexagonal nanopyramidal nanostructures. When the supply of Zn(g) is decreased, crystal growth on the non-polar surfaces (parallel to the *c*-axis) is greatly affected, while growth on the polar (001) surface is less affected due to its faster crystal growth rate. Therefore, the overall diameter of a hexagonal pillar decreased over time resulting in a pyramidal structure. The step-wise morphology is derived from the Ehrlich–Schwöebel (ES) barrier mechanism,[29,30] which is an atomic scale energy barrier against interlayer transport at the edge of the terrace. Since the ES barrier is known to be a very small value, it can be neglected under high temperature conditions, but it becomes noticeable in a low temperature process.[31] During the crystal growth process, the surface energy is further increased when another layer is formed on top of the previous layer, while the previous layer is not fully occupied. Therefore, a layer-by-layer growth mechanism is favored to avoid the less stable state. However, the newly nucleated precursor on top of the uncompleted layer has to overcome the ES barrier to migrate to the previous layer. In our experiment, because the kinetic and thermodynamic energy of the adsorbed precursor is low due to low-temperature conditions (only 30 K above the melting point), it occasionally failed to overcome the ES barrier and formed a new layer with a smaller diameter than the previous layer. As the result of the decreasing Zn precursor supply and ES barriers, the ZnO was formed in a step-wise tapered structure. The ZnO nanopyramids were grown with a slightly tilted angle due to the rough surface (41.5 nm RMS surface roughness) of the FTO substrate (Fig. S1†). Since the surface morphology of the FTO substrate is not flat, the ZnO crystal seeds were formed on the tilted surface, which caused the random crystal orientation of the nanopyramids.

The mechanical stability of the ZnO nanopyramids was tested by ultrasonication, as described in the ESI† (Fig. S2). Ultrasonication was chosen because it is a versatile process used to free and separate nanostructures for sample preparation and characterization, but it is powerful enough to break ZnO nanostructures such as nanosheets, nanodisks and nanorods.[32,33] Since ZnO nanostructures are known to be broken apart by ultrasonication, a sample of ZnO nanorods was compared against a sample of ZnO nanopyramids.

Crystal structure

The crystal structure of the synthesized ZnO nanopyramids was studied by XRD pattern analysis. As shown in Fig. 2, there are two sets of peaks, one from the ZnO nanopyramid product (with indexed reflections) and the other from the FTO substrate (black line). In the as-synthesized ZnO nanopyramids (red line), the highest peak intensity was found at 2θ = 34.7°

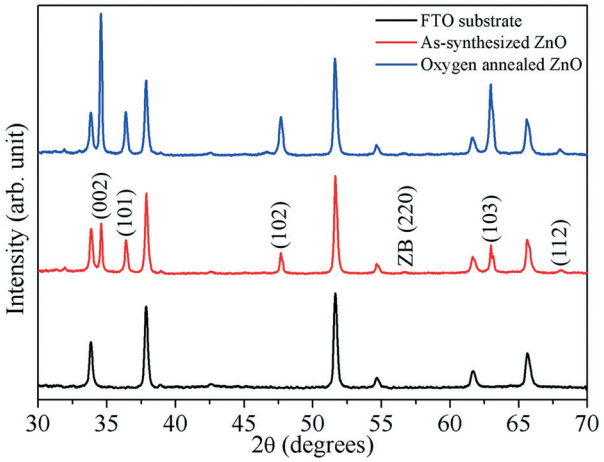

Fig. 2 XRD patterns of the FTO substrate (black), as-synthesized ZnO (red) and ZnO after oxygen annealing (blue). The peaks from ZnO are marked with miller indices. ZB denotes the zinc blende structure.

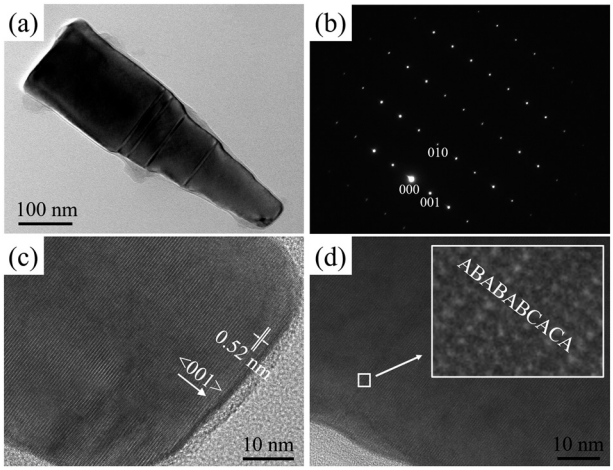

Fig. 3 (a) TEM image of a ZnO nanopyramid; (b) [100] zone axis SAED pattern from the crystal shown in (a), reflections are indexed. The 001 forbidden reflection appeared due to multiple diffraction effects. (c) HRTEM of the top of the pyramid; (d) HRTEM of the stacking fault.

which corresponds to the (002) plane. These results show that the synthesized ZnO nanopyramids are highly crystalline structures and preferentially elongated parallel to the *c*-axis direction. Such a crystal shape leads to dominance of crystal lattice planes normal to the *c*-axis, such as (002), and reduction of the relative number of planes parallel to the *c*-axis as well as pyramidal-type lattice planes. After the oxygen annealing (blue line), the peak intensity from (002) increased significantly, indicating that the crystal grew preferentially along the *c*-axis during the oxygen annealing process, further increasing the preferential development of lattice planes normal to the growth direction. Also, the peak intensities from (101), (102), (103) and (112) increased slightly, providing further evidence that the overall crystallinity of the ZnO nanopyramids was increased by the oxygen annealing.[34]

Detailed analysis of the crystal structure was performed by TEM. Fig. 3a shows a TEM image of a synthesized ZnO nanopyramid. The corresponding selected area electron diffraction (SAED) pattern along [100] shown in Fig. 3b confirms the single crystal nature of the particle and its wurtzite-type structure. The high-resolution transmission electron microscopy (HRTEM) of the synthesized ZnO at the top of the pyramidal structure and the presence of a stacking fault are shown in Fig. 3c and d, respectively. TEM analysis shows that the individual ZnO particle represents a single crystal with a highly ordered wurzite-type structure. The *d*-spacing of 0.52 nm corresponds to the (001) crystal lattice plane of ZnO wurtzite. Planar defects in the form of stacking faults created an isolated layer of a zinc blende structure, one of the polymorphs of ZnO. The presence of isolated zinc blende layers is confirmed by a small XRD peak at 2θ = 56.64° from the (220) crystal plane in the cubic form of ZnO.

Piezoelectric property

AFM and PFM were performed to characterize the piezoelectricity of the synthesized ZnO nanopyramids. To minimize undesired effects during PFM measurements due to crystal orientation[35] and diameter dependency,[36] the characterization of d_{33} was conducted at the apex of vertically standing and not on aggregated pyramids. To improve the piezoelectric performance, the as-synthesized nanopyramids were annealed under an oxygen-rich environment. The surface AFM topography of the annealed ZnO nanopyramids is shown in Fig. 4a and its corresponding 3-D image is shown in Fig. 4b. The point marked with a cross in Fig. 4a and the arrow in Fig. 4b show the location where the piezoresponse measurement was taken. The schematic drawing of the PFM measurement system is illustrated in Fig. 4c.

The results of the PFM measurements are shown in Fig. 5. Fig. 5a shows the applied voltage bias profile, Fig. 5b shows the measured piezoelectric responsive amplitude change against the applied voltage bias, and Fig. 5c shows the piezoelectric response as the voltage bias is swept from −6.0 V to 6.0 V. The synthesized ZnO nanopyramids show a linear piezoelectric contraction response from an applied bias of −6.0 V to +1.4 V, as shown in Fig. 5c. Under an external voltage bias of +1.4 V to 2.0 V, the height of the pyramidal ZnO

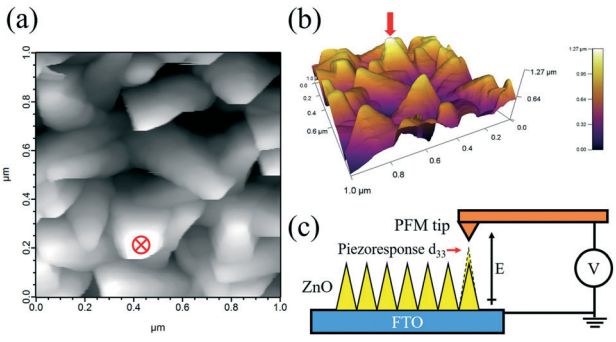

Fig. 4 AFM imaging of the synthesized ZnO nanopyramids: (a) surface topography, (b) 3-D topography, and (c) schematic of PFM measurement.

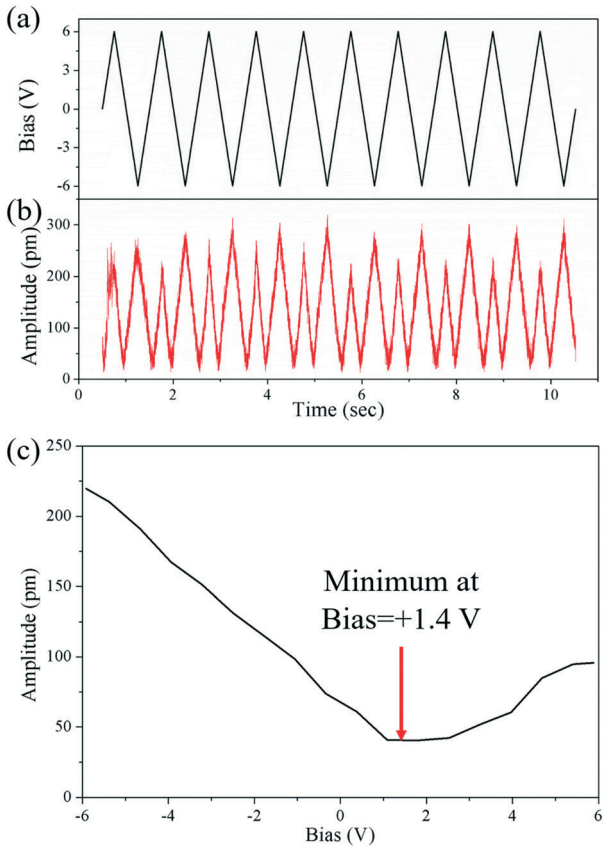

Fig. 5 Piezoelectric response of the synthesized ZnO at the top of a pyramidal structure: (a) input bias, (b) piezoresponse amplitude, and (c) amplitude *vs.* bias curve.

wurtzite nanostructures is at their minimum measured value, and a symmetrical piezoelectric behavior centered on this voltage bias range is observed. In this range, the piezoresponse amplitude is minimum due to the minimized atomic displacement (away from the ideal wurtzite crystal structure). When the voltage bias is increased beyond this range, atomic displacement starts to occur in an opposite manner along the same axis (compared to the −6.0 V to +1.4 V voltage bias sweep), and the ZnO nanopyramids start to re-expand. When the bias is higher than +2.0 V and below +6.0 V, the amplitude of the piezoelectric response increases linearly with the opposite slope in comparison with the −6.0 V to +1.4 V range. The triangular signal (Fig. 5a) produces the piezoelectric amplitude response shown in Fig. 5b. The nanopyramids show a symmetric amplitude change whether the bias is decreased/increased below or above the +1.4–2.0 V voltage bias range. Therefore, the ZnO nanopyramids can be used for two different piezoelectric operations: symmetric and linear. Furthermore, an important aspect of this result is that it plays the role of a signal frequency doubler as a single element. The input signal has a frequency of 1 Hz and the output signal has a frequency of 2 Hz, as shown in Fig. 4a and b, respectively.

The piezoelectric charge coefficient can be calculated using eqn (1):

$$d_{33} = A/VQ \quad (1)$$

where A is the amplitude and V is the voltage bias applied. Q is the quality factor of the PFM cantilever, a dimensionless parameter in oscillation systems used to quantify underdamping in a resonant element. Using this equation, the highest d_{33} from 11 different locations is measured to be 26.10 pm V^{-1} (23.08 pm V^{-1} average) for the oxygen annealed ZnO nanopyramids, while the highest d_{33} in the as-synthesized ZnO nanostructures is measured to be 13.20 pm V^{-1} (10.58 pm V^{-1} average). The statistics from the measurements of the piezoelectric coefficient are shown in Fig. S3.† The annealing process increases the piezoelectric coefficient by 98%. It is expected that crystal defects derived from insufficient oxygen such as V_O or Zn_i are diminished with the annealing process under an oxygen-rich condition. Point crystal defects act as a polarization quencher of the piezoelectric effect because the created dipole moment can be trapped at the defect site, resulting in a lower piezoelectric efficiency of the as-synthesized ZnO.[37] Further evidence of the increase in the crystallinity of the ZnO nanostructures is the observed reduction of planar defects. Although d_{14} of zinc blende and d_{33} of wurtzite ZnO have the same directions, the former has a lower value than the latter.[38] The annealing process allows for the relaxation of the stacking fault leading to the phase transition from zinc blende to wurtzite. This results in an increase in d_{33}, consistent with the phase transition.

Raman spectroscopy

The effect of annealing on the crystal defects of the as-synthesized ZnO nanostructures is analyzed by Raman spectroscopy. The ZnO nanopyramids have a hexagonal wurtzite structure and a C_{6v} symmetry. Four atoms in the unit cell produce 9 optical and 3 acoustic phonon vibration modes, $2A_1 + 2B_1 + 2E_1 + 2E_2$. Among the 12 vibration modes, A_1, E_1 and E_2 are Raman active phonon vibration modes.[39] The Raman spectra of the synthesized ZnO nanopyramids before (black) and after (red) annealing are shown in Fig. 6. The two distinguishable peaks from E_2 vibration can be found at 439 cm^{-1} and 99 cm^{-1}. The peak intensity increased and the full-width-half-maximum (FWHM) decreased (from 1.97 to 1.90 at 99 cm^{-1} and from 8.11 to 7.78 at 439 cm^{-1}) for both peaks. The presence of crystal defects broadens peaks and reduces their intensity, so this observation is evidence that the crystal defect concentration was reduced by oxygen annealing.[40] A noticeable difference before and after the oxygen annealing was found in the range of 500–600 cm^{-1}. A broad peak centered at 552 cm^{-1} was significantly reduced after the oxygen annealing. The peak at 552 cm^{-1} can be assigned as A_1 (LO)[41,42] while the peak at 519 cm^{-1} is not clearly identified because it is related to a multi-phonon process.[43] It has been reported that the presence of a peak is due to oxygen vacancies, deficiencies and incomplete Zn oxidation.[44,45] Therefore, the diminishing of the peak after oxygen annealing is further proof of crystal defect reduction.

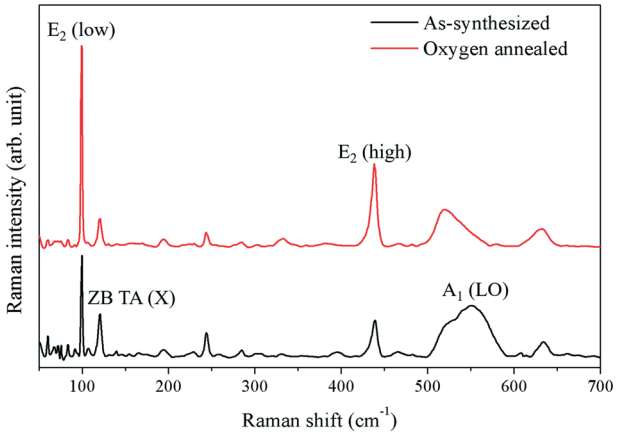

Fig. 6 Raman spectra of ZnO before (black) and after (red) oxygen annealing.

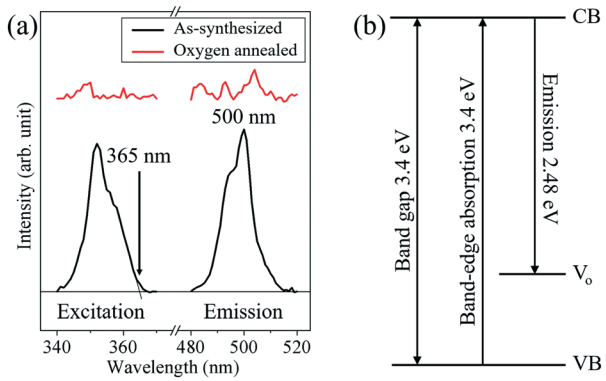

Fig. 7 (a) Photoluminescence spectra of the as-synthesized (black) and oxygen annealed (red) ZnO; (b) energy diagram of the corresponding electron transition in as-synthesized ZnO.

Planar defects forming the zinc blende layer as observed in TEM were also confirmed by Raman spectroscopy at 121 cm^{-1}. The peak is assigned as TA (X)[46] and its intensity decreased after the annealing. The Raman spectroscopic analysis concludes that the point and planar crystal defects were decreased through the annealing under oxygen-rich annealing conditions, resulting in the overall improvement of the ZnO nanopyramid crystallinity.

Photoluminescence spectroscopy

In addition to the Raman spectroscopy, the existence of oxygen vacancies and the oxygen annealing effect reducing the oxygen vacancies are supported by PL spectroscopy, as shown in Fig. 7a. The as-synthesized ZnO nanopyramids absorb UV light shorter than 365 nm (corresponding to the band gap energy of ZnO) and emit green emission at 500 nm (2.48 eV). The UV absorption and green emission are due to the electron transition from the valence band (VB) to the conduction band (CB), and the CB to the oxygen vacancy level,[47] as shown in Fig. 7b. The green emission is not observed after the oxygen annealing.

Conclusions

In conclusion, we successfully synthesized and characterized the piezoelectric response of an array of vertically aligned ZnO hexagonal nanopyramids on a transparent electrode substrate. The tapered morphology of ZnO could be obtained by controlling the premature oxidation of the Zn precursor by isolating the precursor from oxygen gas. The piezoelectric response of the ZnO was measured with PFM, showing 26.10 pm V^{-1} (an improvement of 98%) after oxygen annealing. The effect of the annealing process was analyzed with Raman spectroscopy. It was demonstrated that annealing under an oxygen-rich environment reduced the crystal defects and increased the crystallinity, resulting in better performance in terms of piezoelectric response. The piezoelectric vertically aligned pyramidal ZnO array opens a wide variety of opportunities for piezoelectric applications. The unique characteristics of mechanical stability from its stable architecture and transparency from its wide band gap nature are promising for future applications. Future work will involve a detailed study on defect control, by analyzing the evolution mechanism of defects and determining the overall effect of defects on the piezoelectric performance of ZnO nanopyramids.

Conflicts of interest

There are no conflicts of interest to declare.

Acknowledgements

Electron microscopy was performed using the Nova NanoSEM 450 in CFAMM at UC Riverside. This research was partially supported by a grant from UC Solar MR-15-328386.

Notes and references

1 J. A. Johnson, J. J. Heidenreich, R. A. Mantz, P. M. Baker and M. S. Donley, *Prog. Org. Coat.*, 2003, **47**, 432–442.
2 R. H. Wang, J. H. Xin and X. M. Tao, *Inorg. Chem.*, 2005, **44**, 3926–3930.
3 A. Sugunan, V. K. Guduru, A. Uheida, M. S. Toprak and M. Muhammed, *J. Am. Ceram. Soc.*, 2010, **93**, 3740–3744.
4 X. Hu, Y. Masuda, T. Ohji and K. Kato, *J. Am. Ceram. Soc.*, 2010, **93**, 881–886.
5 D. J. Gargas, M. E. Toimil-Molares and P. Yang, *J. Am. Chem. Soc.*, 2009, **131**, 2125–2127.
6 Y. He, W. Zhang, S. Zhang, X. Kang, W. Peng and Y. Xu, *Sens. Actuators, A*, 2012, **181**, 6–12.
7 Z. P. Wei, Y. M. Lu, D. Z. Shen, Z. Z. Zhang, B. Yao, B. H. Li, J. Y. Zhang, D. X. Zhao, X. W. Fan and Z. K. Tang, *Appl. Phys. Lett.*, 2007, **90**, 042113.
8 R. M. Martin, *Phys. Rev. B: Solid State*, 1972, **5**, 1607–1613.
9 L. Dong and S. P. Alpay, *Phys. Rev. B: Condens. Matter Mater. Phys.*, 2011, **84**, 035315.
10 S. H. Lee, S. S. Lee, J.-J. Choi, J. U. Jeon and K. Ro, *Microsyst. Technol.*, 2005, **11**, 416–423.

11 B. Hadimioglu, L. J. La Comb, D. R. Wright, B. T. Khuri-Yakub and C. F. Quate, *Appl. Phys. Lett.*, 1987, **50**, 1642–1644.
12 G.-A. Racine, P. Muralt and M.-A. Dubois, *Smart Mater. Struct.*, 1998, **7**, 404–416.
13 M. Riaz, J. Song, O. Nur, Z. L. Wang and M. Willander, *Adv. Funct. Mater.*, 2011, **21**, 628–633.
14 M. Ahmad, M. A. Iqbal, J. Kiely, R. Luxton and M. Jabeen, *J. Phys. Chem. Solids*, 2017, **104**, 281–285.
15 A. L. Kholkin, E. L. Colla, A. K. Tagantsev, D. V. Taylor and N. Setter, *Appl. Phys. Lett.*, 1996, **68**, 2577–2579.
16 X. Y. Kong and Z. L. Wang, *Appl. Phys. Lett.*, 2004, **84**, 975–977.
17 M. J. Schulz, M. J. Sundaresan, J. Mcmichael, D. Clayton, R. Sadler and B. Nagel, *J. Intell. Mater. Syst. Struct.*, 2003, **14**, 693–705.
18 I. B. Kobiakov, *Solid State Commun.*, 1980, **35**, 305–310.
19 C. Pan, L. Dong, G. Zhu, S. Niu, R. Yu, Q. Yang, Y. Liu and Z. L. Wang, *Nat. Photonics*, 2013, **7**, 752–758.
20 P. Wang, Y. Fu, B. Yu, Y. Zhao, L. Xing and X. Xue, *J. Mater. Chem. A*, 2015, **3**, 3529–3535.
21 Z. L. Wang, *Science*, 2006, **312**, 242–246.
22 X. Q. Zhang, *et al.*, *J. Phys.: Condens. Matter*, 2003, **15**, 5191.
23 P. Hiralal, H. E. Unalan and G. A. J. Amaratunga, *Nanotechnology*, 2012, **23**, 194002.
24 R. Yang, Y. Qin, L. Dai and Z. L. Wang, *Nat. Nanotechnol.*, 2009, **4**, 34–39.
25 T. Lim and A. Martinez-Morales, in *Materials Research Society Symposium Proceedings*, Materials Research Society, 2015, pp. 35–40.
26 N. Jedrecy, S. Gallini, M. Sauvage-Simkin and R. Pinchaux, *Surf. Sci.*, 2000, **460**, 136–143.
27 L. Qiao, Y. Zeng, C. Q. Qu, H. Z. Zhang, X. Y. Hu, L. J. Song, D. M. Bi and S. J. Liu, *Phys. E*, 2013, **48**, 7–12.
28 C. R. Gorla, N. W. Emanetoglu, S. Liang, W. E. Mayo, Y. Lu, M. Wraback and H. Shen, *J. Appl. Phys.*, 1999, **85**, 2595–2602.
29 R. L. Schwoebel and E. J. Shipsey, *J. Appl. Phys.*, 1966, **37**, 3682–3686.
30 G. Ehrlich and F. G. Hudda, *J. Chem. Phys.*, 1966, **44**, 1039–1049.
31 F. F. Leal, S. C. Ferreira and S. O. Ferreira, *J. Phys.: Condens. Matter*, 2011, **23**, 292201.
32 A. Umar and Y. B. Hahn, *Nanotechnology*, 2006, **17**, 2174–2180.
33 F. Fang, J. Futter, A. Markwitz and J. Kennedy, *Nanotechnology*, 2009, **20**, 245502.
34 Z. B. Fang, Z. J. Yan, Y. S. Tan, X. Q. Liu and Y. Y. Wang, *Appl. Surf. Sci.*, 2005, **241**, 303–308.
35 D. Damjanovic, F. Brem and N. Setter, *Appl. Phys. Lett.*, 2002, **80**, 652–654.
36 R. Agrawal and H. D. Espinosa, *Nano Lett.*, 2011, **11**, 786–790.
37 H. S. Lee and T. Kimura, *J. Am. Ceram. Soc.*, 1998, **81**, 3228–3236.
38 M. Catti, Y. Noel and R. Dovesi, *J. Phys. Chem. Solids*, 2003, **64**, 2183–2190.
39 F. Decremps, J. Pellicer-Porres, A. M. Saitta, J.-C. Chervin and A. Polian, *Phys. Rev. B: Condens. Matter Mater. Phys.*, 2002, **65**, 092101.
40 Q. Zhao, X. Y. Xu, X. F. Song, X. Z. Zhang, D. P. Yu, C. P. Li and L. Guo, *Appl. Phys. Lett.*, 2006, **88**, 033102.
41 S. H. Huang, Z. Chen, X. C. Shen, Z. Q. Zhu and K. Yu, *Solid State Commun.*, 2008, **145**, 418–422.
42 A. Zaoui and W. Sekkal, *Phys. Rev. B: Condens. Matter Mater. Phys.*, 2002, **66**, 174106.
43 B. Cheng, Y. Xiao, G. Wu and L. Zhang, *Appl. Phys. Lett.*, 2004, **84**, 416–418.
44 A. Phuruangrat, O. Yayapao, S. Thongtem and T. Thongtem, *Russ. J. Phys. Chem. A*, 2016, **90**, 949–954.
45 J. Ye, S. Gu, S. Zhu, T. Chen, W. Liu, F. Qin, L. Hu, R. Zhang, Y. Shi and Y. Zheng, *J. Vac. Sci. Technol., A*, 2003, **21**, 979–982.
46 Y. Yu, J. Zhou, H. Han, C. Zhang, T. Cai, C. Song and T. Gao, *J. Alloys Compd.*, 2009, **471**, 492–497.
47 F. Gallino, G. Pacchioni and C. Di Valentin, *J. Chem. Phys.*, 2010, **133**, 144512.

